Nanoscale



PAPER View Journal | View Issue



Cite this: Nanoscale, 2023, 15, 8181

Metal-organic framework-derived trimetallic oxides with dual sensing functions for ethanol†

Xin-Yu Huang, page Ya-Ru Kang, Shu Yan, page Ahmed Elmarakbi, page Yong-Qing Fu strand Wan-Feng Xie strand **Cong-Qing Fu strand **Cong-Ruing Fu strand **Cong-R

Metal-organic framework (MOF)-derived metal oxide semiconductors have recently received extensive attention in gas sensing applications due to their high porosity and three-dimensional architecture. Still, challenges remain for MOF-derived materials, including low-cost and facile synthetic methods, rational nanostructure design, and superior gas-sensing performances. Herein, a series of Fe-MIL-88B-derived trimetallic FeCoNi oxides (FCN-MOS) with a mesoporous structure were synthesized by a one-step hydrothermal reaction followed by calcination. The FCN-MOS system consists of three main phases: α -Fe₂O₃ (n-type), CoFe₂O₄, and NiFe₂O₄ (p-type), and the nanostructure and pore size can be controlled by altering the content of α -Fe₂O₃, CoFe₂O₄, and NiFe₂O₄. The sensors based on FCN-MOS exhibit a high response of 71.9, a good selectivity towards 100 ppm ethanol at 250 °C, and long-term stability up to 60 days. Additionally, the FCN-MOS-based sensors show a p-n transition gas sensing behavior with the alteration of the Fe/Co/Ni ratio.

Received 22nd February 2023, Accepted 2nd April 2023 DOI: 10.1039/d3nr00841j

rsc.li/nanoscale

Introduction

Metal-organic frameworks (MOFs), a network with a three-dimensional porous structure and a large specific surface area, are constructed *via* coordination bonds between inorganic nodes and organic ligands. ¹⁻⁴ Compared to the most MOFs containing divalent metal cations, Fe-MOFs are more robust porous frameworks linked by trivalent metals. ⁵ Among the well-known Fe³⁺-terephthalate MOFs, Fe-MIL-88B is a flexible framework with a three-dimensional hexagonal structure and exhibits continuous breathing during solvation/desolvation. ^{6,7} Considering the outstanding nature of MOFs, recently, tremendous attention has been paid to the development of MOF-derived metal oxide semiconductors (MOSs). ^{8,9} MOF-derived MOS materials exhibit multifunctional characteristics and have been utilized in various applications such as catalysis, ¹⁰ oxygen evolution reactions, ^{11,12} and ion batteries. ¹³

In the past few decades, various gas sensors have been developed for monitoring different gases. Among them, chemi-

To date, many polymetallic oxides have been developed for gas sensing using bimetallic or trimetallic MOFs as templates. Introducing different metal ions into MOF-derived MOS systems can effectively increase their active sites and conductivity, leading to an improvement of the physicochemical reaction rates of target analytes. 18,19 Accordingly, Fe-MIL-88B-derived polymetallic oxides are promising candidates to enhance gas sensing. Typically, the direct sacrifice of Fe-MIL-88B can obtain the monometallic oxide of α -Fe₂O₃, an n-type semiconductor with a bandgap (E_g) of 2.2 eV, which is often utilized for chemiresistive gas sensors. 17 By doping the Fe-MIL-88B template with heteroatoms of similar periods, polymetallic oxides consisting of MFe₂O₄-based spinels can be formed. (M = Ni, Co, Zn, and Mn). Furthermore, MFe₂O₄-based spinels also show good gas-sensing performance. 17 Among

resistive sensors are widely used for gas detection, owing to their portable and low-cost properties. ^{14,15} Most chemiresistive sensors are MOS-based and operate at relatively high temperatures (typically around 300 °C) to achieve better sensing performances. ^{16,17} However, MOFs cannot remain stable at such high temperatures because of the poor thermal stability of their organic skeleton. Besides, it is hard to effectively obtain the sensing signal of MOFs due to their poor electrical conductivity, and a few studies directly applied MOFs on chemiresistive sensors. To overcome the above limitation, it is feasible and promising to utilize MOF-derived MOSs as sensing materials, which can effectively optimize the nanostructure and increase the active sites of sensing materials, thus improving the gas-sensing performance further.

^aCollege of Electronics and Information, University-Industry Joint Center for Ocean Observation and Broadband Communication, Qingdao University, Qingdao 266071, P. R. China. E-mail: wfxie@qdu.edu.cn

^bSchool of Integrated Circuits, University of Chinese Academy of Sciences, Beijing 100049. P. R. China

^cFaculty of Engineering and Environment, Northumbria University, Newcastle upon Tyne NE1 8ST, UK. E-mail: richard.fu@northumbria.ac.uk

^dDepartment of Physics, Dongguk University, Seoul 04620, South Korea

[†] Electronic supplementary information (ESI) available. See DOI: https://doi.org/10.1039/d3nr00841i

Paper

them, CoFe₂O₄ and NiFe₂O₄ spinel oxides, which are widely applied in chemiresistive gas sensors, are p-type semiconductor materials with bandgaps of 0.8 and 1.3 eV, respectively.20,21 For example, double-shelled nanocubes of Co₃O₄/CoFe₂O₄ show a response of 12.7 toward 10 ppm formaldehyde with a fast response/recovery speed (4/9 s) and an LOD of 300 ppb;²² hierarchically double-shelled hollow spheres of CoFe₂O₄ exhibit high sensitivity to ammonia gas at 240 °C;²⁰ superfine and porous NiFe2O4 microspheres exhibit a high selectivity to acetone against other interfering gases, with a sensitivity of 27.4, an LOD of 200 ppb, and a fast response time of 2 s towards 100 ppm acetone; ²³ α-Fe₂O₃/NiFe₂O₄ nanotubes with a large specific surface area (118.03 m² g⁻¹) exhibit excellent sensing performance, including good sensitivity (23), a fast response speed (4 s), and long-term stability (30 days) towards 100 ppm acetone at 200 °C.24 Hence, it is worthwhile

to develop α-Fe₂O₃, CoFe₂O₄, and NiFe₂O₄ nanocomposites as

gas-sensing materials by using the Fe-MOF template doped

In this work, a series of Fe-MIL-88B-derived trimetallic FeCoNi metal oxide semiconductors (FCN-MOS) with a mesoporous nanostructure were successfully synthesized by a onestep hydrothermal reaction followed by calcination treatment. By optimizing the ratio of α -Fe₂O₃ and MFe₂O₄ in the FCN-MOS system, the nanostructure and pore size can be effectively tuned, resulting in the enhancement of gas-sensing performance. The FCN-MOS with the optimal molar ratio (Fe: Co: Ni = 7: 1.5: 1.5) has an elongated hexagonal rod-like structure with abundant mesopores and a large specific area. The sensor based on $Fe_7Co_{1.5}Ni_{1.5}$ shows high sensitivity (S = 71.9), long-term stability, and good selectivity for ethanol at the optimal working temperature of 250 °C. Besides, an interesting p-n gas-sensing transition behavior was observed when varying the Fe/Co/Ni ratio, and the sensing mechanism was fully discussed.

Experimental

Synthesis of FCN-MOSs

with Co and Ni heteroatoms.

All the chemicals were purchased from Aladdin Industrial Corporation and used without purification. These include ferric trichloride (FeCl₃·6H₂O), cobalt(Π) acetate tetrahydrate (Co(Ac)₂·4H₂O), nickel(Π) acetate tetrahydrate (Ni(Ac)₂·4H₂O), p-phthalic acid (1,4-BDC), N,N-dimethylformamide (DMF), acetone (C₃H₆O), and ammonia (NH₃·H₂O).

A series of MOF-derived MOSs were synthesized using a hydrothermal method with the following calcination treatment. Generally, 1 mmol of $FeCl_3 \cdot 6H_2O$ was dissolved in 20 mL of a mixed solvent of DMF and acetone (with a volume ratio of 1:1) to form solution A. 1 mmol of 1,4-BDC was dissolved in 10 ml of a mixed solvent of DMF and acetone (volume ratio is 1:1) to form solution B. Then, solution A was poured into solution B and magnetically stirred for 1 h at room temperature, while adding 100 μ L of ammonia solution. The mixed solution was poured into a Teflon-lined stainless-

steel autoclave (50 mL) and was heated to 120 °C for 24 h. The obtained products were washed with deionized water and absolute ethanol three times, followed by centrifugation, and then dried at 70 °C for 12 h in an oven. Finally, the samples were calcined in a muffle furnace at 500 °C for 3 h in an ambient environment. The calcined products were collected for analysis. Similarly, other types of FCN-MOSs were also prepared using the same procedures but with different Fe, Co, and Ni ratios. For convenience, these FCN-MOSs of $Fe_7Co_{1.5}Ni_{1.5}$, $Fe_6Co_2Ni_2$, $Fe_4Co_4Ni_2$ and $Fe_2Co_6Ni_2$ were named according to their molar ratios of 7:1.5:1.5, 6:2:2, 4:4:2 and 2:6:2 of $FeCl_3\cdot 6H_2O$ $/Co(Ac)_2\cdot 4H_2O/Ni(Ac)_2\cdot 4H_2O$, respectively.

Sensor fabrication and measurement

For sensing layers, first, FCN-MOSs (including Fe₇Co_{1.5}Ni_{1.5}, Fe₆Co₂Ni₂, Fe₄Co₄Ni₂, and Fe₂Co₆Ni₂) were grounded thoroughly in ethanol in an agate mortar to obtain a homogeneous paste, which was uniformly coated onto the surface of an alumina ceramic tube and dried at 70 °C under vacuum for 12 h to form a gas-sensing layer. Gas-sensing tests were performed using a WS-30A gas-sensing measurement system (Zhengzhou Winsen Electronic Technology Co., Ltd, China). During the tests, the target gases with the given concentrations were injected into the evaporation platform of a test chamber (18 L) via a micro syringe. The substrate platform was heated to evaporate the liquid target analyte, and then the targeted gas was evenly distributed in the test chamber after diffusion using an air circulation device. When the resistance reading of the sensor became stable, the test chamber was lifted open to introduce the ambient air. The response (S) of the gas sensor can be calculated from $S = R_a/R_g$ (n-type) or $S = R_g/R_a$ (p-type), where R_a and R_g represent the resistance values of the sensor in air and in the testing gases, respectively.

Characterization

The surface morphology of the synthesized FCN-MOSs was characterized using a field emission scanning electron microscope (FE-SEM, Zeiss Gemini 500, Germany). Elemental mapping of the samples was performed using an energy-dispersive X-ray spectroscope (EDS, Oxford Link-ISIS 300, UK) operated at 15 kV. Crystal structures of the FCN-MOSs were high-resolution transmission microscopy (HR-TEM, JEOL-2100 F, Japan), and interplanar spacings of lattice fringes were obtained using data analysis software (Gatan Digital Micrograph, USA). X-ray diffraction (XRD) was used to study the crystalline structure of the FCN-MOSs and was carried out using a Bruker D8 diffractometer equipped with Cu K α radiation ($\lambda = 0.154$ nm). X-ray photoelectron spectroscopy (XPS) was used to determine the surface elemental composition and the chemical state of bonds of the FCN-MOSs, and an Escalab 250xi instrument (Thermo Scientific, USA) equipped with a monochromatic Al $K\alpha$ source was used. The specific surface area and the pore size were determined by nitrogen (N2) adsorption-desorption measurement using Brunner-Emmett-Teller

Nanoscale Paper

Barrett-Joyner-Halenda (BJH) methods (Autosorb iQ Station 1, USA).

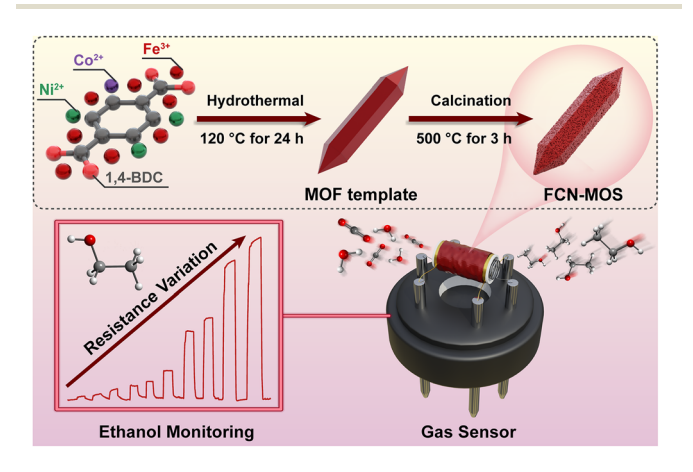
Results and discussion

Characterization of FCN-MOSs

In this work, MOF-derived MOS materials were synthesized via a one-step hydrothermal method and after calcination treatment using the Fe-MIL-88B template. A series of FeCoNi-trimetallic oxides were obtained, and the overall design and implementation processes are systematically illustrated in Scheme 1.

The morphologies of the Fe-MIL-88B template and its derivative were characterized by FE-SEM. The SEM images in Fig. S1[†] indicate that Fe-MIL-88B is a well-defined uniform hexagonal rod with pointed ends, which is consistent with previous reports. 25,26 The SEM images of Fe₇Co_{1.5}Ni_{1.5} (Fig. 1a-c) show that the sample possesses an elongated hexagonal rod structure with an average length of 587 nm (Fig. S2†), similar to that of the MOF template. Furthermore, it can be observed that many nanoparticles are scattered on the sample surface and accumulate to form mesopores. For comparisons, the surface morphologies of Fe₆Co₂Ni₂, Fe₄Co₄Ni₂, and Fe₂Co₆Ni₂ were also characterized (Fig. S3†). The results reveal that the Fe₆Co₂Ni₂ and Fe₄Co₄Ni₂ samples maintain an elongated hexagonal structure, and the nanoparticle sizes become larger as the Fe/Ni ratios decrease. However, for Fe₂Co₆Ni₂, the structure became amorphous but still consisted of many nanoparticles.

TEM analysis was also performed to further investigate the morphology and structure. As shown in Fig. S4,† the Fe-MIL-88B template has a solid bulky rod-like structure with sharp edges. TEM images of Fe₇Co_{1.5}Ni_{1.5} (Fig. 1d and e) further confirm that the sample is composed of nanoparticles ranging in size from 6 to 18 nm, with an average size of approximately 11 nm (Fig. S5†). The HR-TEM image (Fig. 1f) reveals distinctive spacings of 0.368 and 0.220 nm corresponding to the (012) and (006) lattice planes of α -Fe₂O₃, and



Scheme 1 The formation processes of FCN-MOS materials and the asfabricated sensors.

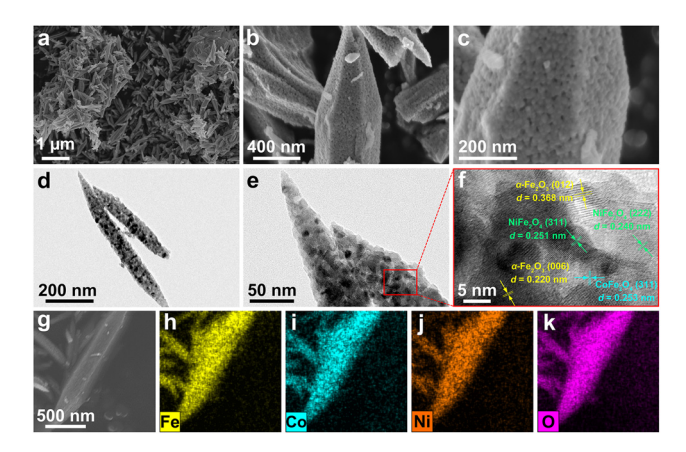


Fig. 1 (a-c) SEM images of Fe₇Co_{1.5}Ni_{1.5} at different magnifications. (df) TEM and HR-TEM images of Fe₇Co_{1.5}Ni_{1.5}. (g) EDS mapping images of (h) Fe, (i) Co, (j) Ni, and (k) O elements distributed at Fe₇Co_{1.5}Ni_{1.5}.

the (222) and (311) lattice planes of NiFe2O4 are 0.251 and 0.240 nm, respectively, whereas that of the (311) lattice plane of CoFe₂O₄ is 0.253 nm. The elements of Fe, Co, Ni, and O (Fig. 1h-k) are consistently distributed across the selected scanning area (Fig. 1g) from the EDS elemental mapping results, demonstrating that the acquired sample is constituted of Fe, Co, Ni, and O elements. The EDS spectrum (Fig. S6†) shows that Fe₇Co_{1.5}Ni_{1.5} contains 39.78% Fe, 1.52% Co and 15.47% Ni in atomic percentage, and the remaining concentration is oxygen.

It is vital to investigate the specific surface area and the pore size distribution of the MOF template and its derivative material. Hence, N2 adsorption-desorption measurements were carried out. Both samples show the H4 isotherm curves (Fig. S7†).²⁷ The specific surface area of Fe-MIL-88B is calculated to be 55.70 m² g⁻¹ (Fig. S7a†) and has a high mesomicroporosity (Fig. S7b†). The sample Fe₇Co_{1.5}Ni_{1.5} has a specific surface area of 39.51 m² g⁻¹ (Fig. S7c†) and a uniform distribution of main mesopores of about 8 nm (Fig. S7d†). The BET and BJH results demonstrate that using MOFs as a template to drive metal oxides can effectively obtain a relatively high specific surface area and abundant mesoporous.

The XRD pattern of the prepared Fe-MIL-88B is shown in Fig. S8,† for which the characteristic peaks correlate well to previous reports, demonstrating the successful synthesis of Fe-MIL-88B. 7,25,26 Fig. 2a indicates that the crystalline phases of α-Fe₂O₃, CoFe₂O₄, and NiFe₂O₄ are detected in Fe₇Co_{1.5}Ni_{1.5}, Fe₆Co₂Ni₂, and Fe₄Co₄Ni₂, without the diffraction peaks of other phases. The observed diffraction peaks can be readily indexed to the crystal planes of α-Fe₂O₃ (PDF#33-0664), CoFe₂O₄ (PDF#03-0864), and NiFe₂O₄ (PDF#54-0964) phases, respectively, which agree well with the values from the powder diffraction file documents (Table S1†). The enlarged pattern in Fig. 2b shows that the intensity of the peak assigned to α -Fe₂O₃ (104) gradually decreases with the Fe/Ni ratio.

As it is well known, α-Fe₂O₃, an n-type sensing material, plays a critical role in enhancing the sensing performance.

Paper Nanoscale

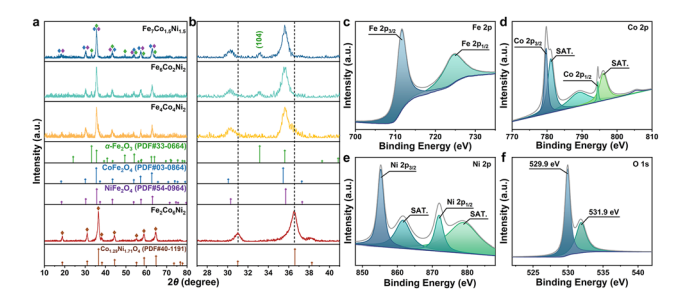


Fig. 2 (a and b) XRD patterns of Fe₇Co_{1.5}Ni_{1.5}, Fe₆Co₂Ni₂, Fe₄Co₄Ni₂, and Fe₂Co₆Ni₂. High-resolution XPS spectra of Fe₇Co_{1.5}Ni_{1.5} for (c) Fe 2p, (d) Co 2p, (e) Ni 2p, and (f) O 1s.

Therefore, the XRD results imply that the high α-Fe₂O₃ ratio of the samples (i.e., Fe₇Co_{1.5}Ni_{1.5} and Fe₆Co₂Ni₂) might have excellent gas sensing properties. However, for the sample of $Fe_4Co_4Ni_2$, as the α - Fe_2O_3 content is reduced with the decrease of Fe element proportion, the sensor based on Fe₄Co₄Ni₂ might exhibit a transition from n-type to p-type sensing behavior accompanied by the deteriorated sensing performance. Nevertheless, it was found that the Fe₂Co₆Ni₂ sample is composed of $Co_{1.29}Ni_{1.71}O_4$ (PDF#40-1191) (Table S1†). The different crystalline structures of Fe₂Co₆Ni₂ are attributed to the relatively low Fe ratio in the FCN-MOS, which results in the absence of the α-Fe₂O₃ phase and the formation of a Co_{1,29}Ni_{1,71}O₄ phase. Therefore, the change in Fe₂Co₆Ni₂ composition leads to morphology and structure conversion, further affecting its gas-sensing properties. XRD pattern of pristine α-Fe₂O₃ is shown in Fig. S9,† corresponding to the phase of α -Fe₂O₃ (PDF#33-0664).

The XPS survey spectrum of Fe₇Co_{1.5}Ni_{1.5} (Fig. 2c-f) shows the peaks of Fe 2p, Co 3d, Ni 3d, and O 1s. In the high-resolution spectrum of Fe 2p (Fig. 2c), two distinct peaks are observed at 711.6 eV for Fe $2p_{3/2}$ and 724.9 eV for Fe $2p_{1/2}$, corresponding to Fe³⁺ ions.²⁸ The energy gap of 13.3 eV between these two peaks is close to the values reported in the standard spectrum of Fe 2p. In the Co 2p spectrum (Fig. 2d), there are two peaks located at 779.7 and 794.5 eV, which are associated with the valence states of Co⁺² for Co 2p_{3/2} and Co 2p_{1/2}, respectively.²⁹ In the Ni 2p spectrum (Fig. 2e), two peaks at 855.2 and 871.9 eV correspond to Ni 2p_{3/2} and 2p_{1/2}, respectively were observed. The Ni²⁺ and Ni³⁺ peaks have two satellite peaks of $2p_{3/2}$ and $2p_{1/2}$ at approximately 861.6 and 878.8 eV.³⁰ The O 1s spectrum (Fig. 2f) contains two peaks centered at 529.9 and 531.9 eV, representing lattice oxygen and chemisorbed oxygen, respectively.31 The existence of chemisorbed oxygen is due to the surface chemisorbed O2 molecules, which is favorable for detecting the response of the target gas molecules.

The sensitivity of the FCN-MOS-based sensors substantially depends on the operating temperature. It is reported that conduction band electrons (e⁻) are dependent on the temperature, doping element, and volume mainly. The excited temperature (T) generates the electron concentration (n_0) in the conductive band (E_c) for a semiconductor material, which is shown in eqn (1):32

$$n_0 = 2 \left(\frac{m_n^* k_0 T}{2\pi \hbar^2} \right)^{\frac{3}{2}} \exp\left(-\frac{E_{\rm C} - E_{\rm F}}{k_0 T} \right)$$
 (1)

where m_n^* is the effective mass of the electron, k_0 is Boltzmann's constant, h is Planck's constant, $\hbar = h/2\pi$, and E_F is the Fermi energy. The higher the temperature, the higher the concentration of electrons. However, for a gas sensor, the sensing performance is not linearly dependent on the temperature. Due to the weak adsorption energy of target gas molecules and oxygen species (O₂⁻, O⁻, and O²⁻) on the surface of the sensing material at a high temperature, chemisorbed target gas molecules and oxygen species would easily escape from the surface of the sensing materials at a higher temperature, which could reduce the sensing catalytic reaction. As a result, it is essential and crucial to investigate the best operating temperature of the as-prepared sensors based on FCN-MOSs.

Gas-sensing performances of sensors based on Fe₇Co_{1.5}Ni_{1.5} and Fe₆Co₂Ni₂

Fig. 3a shows the curves of sensing properties vs. detection temperature, and the sensitivity has no discernible differences at low temperatures (from 50 to 150 °C). Then, the sensitivity increases significantly after 150 °C, with a maximum sensing value occurring at 250 °C. The sensitivities of Fe₇Co_{1.5}Ni_{1.5} and

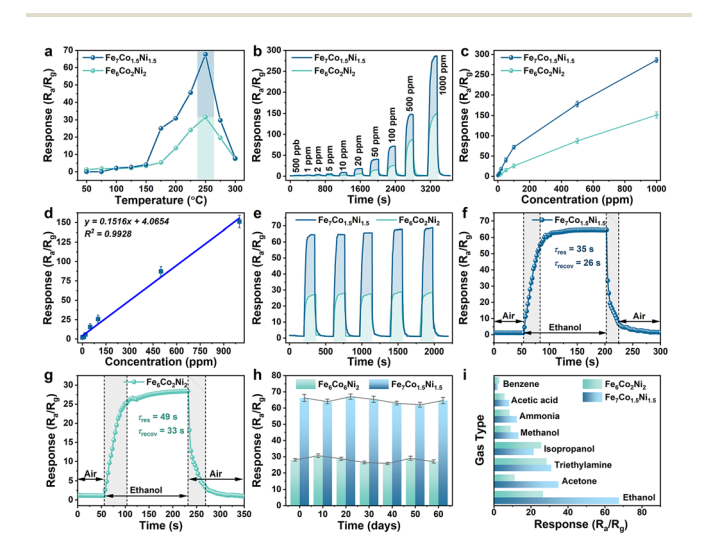


Fig. 3 Gas-sensing measurements: (a) response curves of Fe₇Co_{1.5}Ni_{1.5} and Fe₆Co₂Ni₂ toward 100 ppm ethanol at different operating temperatures. (b) Dynamic response curves of Fe7Co1.5Ni1.5 and Fe6Co2Ni2 toward ethanol from 0.5 to 1000 pm at 250 °C. (c) Curves of response vs. concentration for Fe₇Co_{1.5}Ni_{1.5} and Fe₆Co₂Ni₂. (d) Linear fitting of the response value as a function of ethanol concentration. (e) Reproducibility tests (five periods) of Fe₇Co_{1.5}Ni_{1.5} and Fe₆Co₂Ni₂ toward 100 ppm ethanol at 250 °C. Response/recovery times of (f) $Fe_7Co_{1.5}Ni_{1.5}$ and (g) Fe₆Co₂Ni₂ towards 100 ppm ethanol at 250 °C, respectively. (h) Long-term repeatability tests of $Fe_7Co_{1.5}Ni_{1.5}$ and $Fe_6Co_2Ni_2$ toward 100 ppm ethanol. (i) Selectivity tests of Fe₇Co_{1.5}Ni_{1.5} and Fe₆Co₂Ni₂ toward 100 ppm of different target gases at 250 °C.

Nanoscale **Paper**

Fe₆Co₂Ni₂ show rapid decreases from 250 to 300 °C. Therefore, the optimal operating temperature for the Fe₇Co_{1.5}Ni_{1.5} and Fe₆Co₂Ni₂-based sensors are set at 250 °C.

Dynamic response-recovery curves of Fe₇Co_{1.5}Ni_{1.5} and Fe₆Co₂Ni₂ in the ethanol concentration range from 0.5 to 1000 ppm are shown in Fig. 3b. Both gas sensors show good responses and recovery behaviors with various ethanol concentrations. With the increase of ethanol concentrations, the gas sensor responses exhibit a step-increasing pattern at the optimum working temperature of 250 °C. Compared to the Fe₆Co₂Ni₂ based sensor, the response of Fe₇Co_{1.5}Ni_{1.5} is significantly increased with the concentration of targeted gases. These two sensors do not reach their saturation conditions when the ethanol concentration is 1000 ppm, as shown in Fig. 3c. In summary, the Fe₇Co_{1.5}Ni_{1.5} based sensor has a better response than Fe₆Co₂Ni₂, owing to its optimal metal component ratio of Fe, Co, and Ni and the presence of the α-Fe₂O₃ phase. The LOD of the sensor to ethanol vapor was calculated utilizing a linear extrapolation of response sensitivity as a function of ethanol concentration (Fig. 3d). The calculated LOD result shows an ultra-low ethanol detection concentration of 30.7 ppb for Fe₇Co_{1.5}Ni_{1.5} operated at 250 °C. The repeatability and stability of ethanol sensing were further investigated using Fe₇Co_{1.5}Ni_{1.5} and Fe₆Co₂Ni₂. Fig. 3e shows that after five cycles of exposure to 100 ppm of ethanol at 250 °C, both Fe₇Co_{1.5}Ni_{1.5} Fe₆Co₂Ni₂ show repeatable curves, indicating their good stability. Fig. 3f and g show the response and recovery times of Fe7Co1.5Ni1.5 and Fe6Co2Ni2 exposed to 100 ppm ethanol at 250 °C. The Fe₇Co_{1.5}Ni_{1.5}-based sensor has a response time ($\tau_{\rm res}$) of 35 s, which is faster than that (49 s) of Fe₆Co₂Ni₂. Both sensors need a short time to return to 90% of their original resistance (e.g., Fe₇Co_{1.5}Ni_{1.5} needs 26 s and Fe₆Co₂Ni₂ needs 33 s). Because the thermal energy is generally smaller than the activation energy for desorption, most of the chemical sensors do not show good reversibility, resulting in a prolonged recovery time ($\tau_{\rm recov}$). The long-term stability of Fe₇Co_{1.5}Ni_{1.5} and Fe₆Co₂Ni₂ was tested by exposing 100 ppm ethanol to the device once every ten days, measured at 250 °C for two months. Both the sensors show the preserved 98 percentage of their initial value with good stability after two months (Fig. 3h). Selectivity and cross-responses of these two sensors were investigated at 250 °C by exposing them to benzene (C_6H_6) , acetic acid $(C_2H_4O_2)$, ammonia (NH_3) , methanol (CH₄O), isopropanol (C₃H₈O), trimethylamine (C₃H₉N), acetone (C_3H_6O), and ethanol (C_2H_6O) (all with a fixed volume of 100 ppm). The obtained results are shown in Fig. 3i.

The above results clearly indicate that these two sensors are more sensitive to ethanol than other gases, particularly the Fe₇Co_{1.5}Ni_{1.5}-based sensor. The phase of α -Fe₂O₃ can boost the redox process, whereas Fe₇Co_{1.5}Ni_{1.5} can be applied as a catalyst according to previous reports. 24,33,34 Furthermore, the ethanol sensing properties of the sensor based on pristine α-Fe₂O₃ are shown in Fig. S10.† Fig. S10a† shows the response of α -Fe₂O₃ toward 100 ppm ethanol between 150 and 300 °C. The highest response (6.3) of ethanol gas was detected at 250 °C, indicating that the optimal operating temperature is

250 °C for α-Fe₂O₃, the same as the best working temperature of Fe₇Co_{1.5}Ni_{1.5}. Fig. S10b† shows the dynamic response curves of α-Fe₂O₃ at 250 °C for different ethanol vapor concentrations ranging from 5 to 1000 ppm. The result indicates that the response values of α-Fe₂O₃ increase dramatically with increasing ethanol concentration, especially when the concentration is above 500 ppm. Fig. S10c and d† show the calibration curve of α -Fe₂O₃ at various concentrations. The slope at 0–70 ppm is quite small, with a low response, increasing between 70 and 100 ppm. Generally, the pristine α-Fe₂O₃ based sensor shows poor gas-sensing performances for ethanol. Therefore, the combination of α-Fe₂O₃, CoFe₂O₄, and NiFe₂O₄ provides greater catalytic selectivity for the redox interactions between chemisorbed oxygen and ethanol molecules in the sensing material.

Gas-sensing performances of sensors based on Fe₂Co₆Ni₂ and Fe₄Co₄Ni₂

According to the aforementioned bipolar sensor design approach, the n-type sensing performance could be readily changed to p-type sensing performance by lowering the Fe element in the FCN-MOSs (e.g., Fe₂Co₆Ni₂ and Fe₄Co₄Ni₂).

The response-temperature curves of Fe₂Co₆Ni₂ and Fe₄Co₄Ni₂ toward 100 ppm ethanol operated at temperatures ranging from 50 to 300 °C are shown in Fig. 4a. Obviously, both Fe₂Co₆Ni₂ and Fe₄Co₄Ni₂ showed a p-type sensing behavior at their optimum working temperatures of 100 °C and

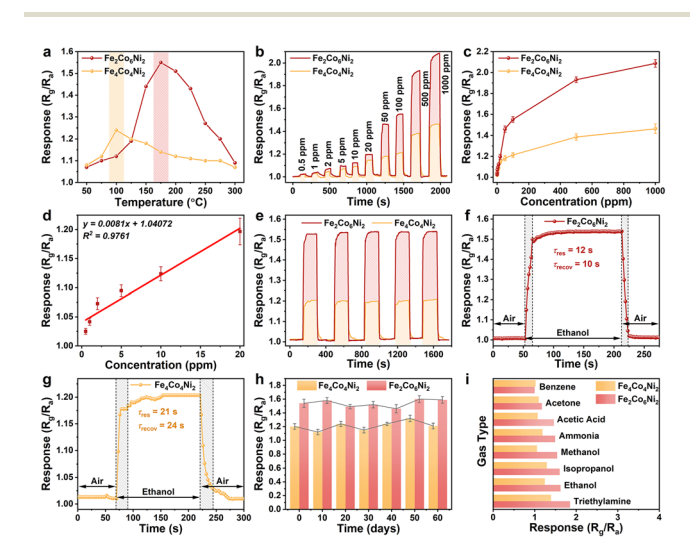


Fig. 4 Gas-sensing measurements: (a) response curves of Fe₂Co₆Ni₂ and Fe₄Co₄Ni₂ toward 100 ppm ethanol at different operating temperatures. (b) Dynamic response curves of Fe₂Co₆Ni₂ and Fe₄Co₄Ni₂ toward ethanol from 0.5 to 1000 pm at 250 °C. (c) Curves of response vs. concentration for Fe₂Co₆Ni₂ and Fe₄Co₄Ni₂. (d) Linear fitting of the response value as a function of ethanol concentration. (e) Reproducibility tests (five periods) of Fe₂Co₆Ni₂ and Fe₄Co₄Ni₂ toward 100 ppm ethanol at 250 °C. Response/recovery times of (f) $Fe_2Co_6Ni_2$ and (g) $Fe_4Co_4Ni_2$ towards 100 ppm ethanol at 250 °C, respectively. (h) Long-term repeatability tests of Fe₂Co₆Ni₂ and Fe₄Co₄Ni₂ toward 100 ppm ethanol. (i) Selectivity tests of Fe₂Co₆Ni₂ and Fe₄Co₄Ni₂ toward 100 ppm of different target gases at 250 °C.

Paper Nanoscale

175 °C. Still, their sensitivity was not as good as Fe₇Co_{1.5}Ni_{1.5} and Fe₆Co₂Ni₂. The responses toward 100 ppm ethanol are 1.54 and 1.21 for these two sensors at their best operation temperatures of 100 °C and 175 °C, respectively. Because of a decrease in the Fe content, the amounts of p-type components in the CoFe₂O₄ and NiFe₂O₄ phases are increased. Therefore, sensors based on Fe₂Co₆Ni₂ and Fe₄Co₄Ni₂ exhibited a p-type sensing behavior.

Fig. 4b shows the dynamic response curves of Fe₂Co₆Ni₂ and Fe₄Co₄Ni₂ to ethanol with its concentration range of 0.5-1000 ppm. The response of Fe₂Co₆Ni₂ is about 1.1 to 1.4 times larger than that of Fe₄Co₄Ni₂. The response values as a function of ethanol concentration are shown in Fig. 4c, and they increase as the ethanol concentration increases. When the concentration is ~20 ppm, the Fe₂Co₆Ni₂ based sensor shows much larger response values. Because of the lower Fe ratio in the FCN-MOSs, Fe₂Co₆Ni₂ shows a more significant response than Fe₄Co₄Ni₂. A linear extrapolation was used to determine the LOD, and the results are shown in Fig. 4d. The obtained LOD for this sensor is 302.6 ppb. The repeatability of Fe₂Co₆Ni₂ and Fe₄Co₄Ni₂ samples' responses to 100 ppm ethanol was also studied for 5 successive cycles, and the results are shown in Fig. 4e. For these two sensors, the obtained curves are nearly identical, with average response values of 1.54 and 1.20, respectively. The responses can be entirely returned to their starting levels in each cycle.

Fig. 4f and g compare the response/recovery times (τ_{res}) $\tau_{\rm recov}$) of Fe₂Co₆Ni₂ and Fe₄Co₄Ni₂ toward 100 ppm ethanol at their optimum working temperatures (i.e., 175 °C for Fe₂Co₆Ni₂ and 100 °C for Fe₄Co₄Ni₂). The Fe₂Co₆Ni₂-based sensor shows a faster response and recovery with its $\tau_{\rm res}/\tau_{\rm recov}$ value of 12/10 s, much shorter than that of Fe₄Co₄Ni₂ (21/24 s). The Fe₂Co₆Ni₂ and Fe₄Co₄Ni₂-based sensors show much shorter $\tau_{\rm res}/\tau_{\rm recov}$ values than those of the Fe₇Co_{1.5}Ni_{1.5} and Fe₆Co₂Ni₂-based sensors, which can be attributed to their relatively lower response values.

The long-term repeatability testing results of Fe₂Co₆Ni₂ and Fe₄Co₄Ni₂ toward 100 ppm ethanol at the optimal testing temperature of 175 $^{\circ}\text{C}$ are shown in Fig. 4h. The sensitivity has not been changed significantly within 60 days, proving the long-term repeatability of Fe₂Co₆Ni₂ and Fe₄Co₄Ni₂.

Fig. 4i presents the selectivity testing results of Fe₂Co₆Ni₂ and Fe₄Co₄Ni₂ when exposed to 100 ppm of various types of gases at their optimal working temperatures. The Fe₂Co₆Ni₂based sensor shows response values of 1.00, 1.17, 1.46, 1.49,

1.54, 1.60, 1.62, and 1.85 for benzene, acetone, acetic acid, ammonia, methanol, isopropanol, ethanol, and triethylamine gases, respectively. The results indicate that sensors based on Fe₂Co₆Ni₂ and Fe₄Co₄Ni₂ have a low selectivity towards ethanol

Discussions on the gas-sensing mechanism

Table 1 compares ethanol sensing performances of various MOF-derived MOS-based sensors reported in the literature, including MOF-derived porous TiO2, MOF-derived CuO, MOFderived Ga-doped Co₃O₄, zirconium-based MOFs, ZIF-67derived Co₃O₄/NiCo₂O₄, and ZIF-8 MOF-derived ZnO. Based on Table 1, our newly developed FCN-MOS-based sensor can be operated at a relatively low working temperature and achieve a faster dynamic response with a higher sensitivity to ethanol. The main reasons are attributed to the novel MOF-derived nanostructures and the optimum proportion of the catalysts of α-Fe₂O₃, CoFe₂O₄, and NiFe₂O₄ phases, which can provide an effective gas diffusion path via a well-aligned porous structure.

Fig. 5 schematically illustrates the adsorption of gas molecules, transfer of electrons, and surface reaction processes of FCN-MOS-derived oxide materials in air and ethanol gases, respectively. Generally, for the n-type sensing mechanism, when a sensing material is exposed to air, oxygen molecules are adsorbed and ionized. Thus, oxygen species such as O₂, O⁻, and O²⁻ exist on the surface. During the oxygen ionization process, the electron concentration in a conductive band (E_c) reduces, then the resistance of the sensing material increases significantly. Therefore, the R_a value is increased. For a p-type sensor, electron extraction would produce a hole accumulation layer near the surface. Accordingly, the R_a value is decreased. Within the detection environment, with the gas such as ethanol in this study, depending on n- or p-types, the thickness of the electron (or hole) accumulation layer decreases (or

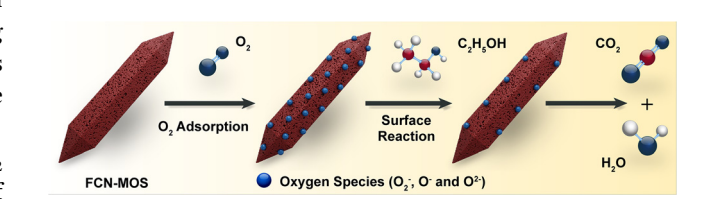


Fig. 5 Schematic diagram of the ethanol gas-sensing mechanism of an FCN-MOS.

Table 1 Comparison between the ethanol sensing performance of MOF-derived MOSs

Materials	Temperature (°C)	Concentration (ppm)	Response (S)	$ au_{ m res}/ au_{ m recov}\left({ m s/s}\right)$
MOF-derived porous TiO ₂ ³⁵	250	500	~46	74/102
MOF-derived CuO ³⁶	275	100	12.1	102/40
MOF-derived Ga-doped Co ₃ O ₄ ³⁷	180	50	~118	3/15
Zirconium-based MOF ³⁸	150	100	~1.4	~50/400
ZIF-67-derived Co ₃ O ₄ /NiCo ₂ O ₄ ³⁹	180	100	26	~4/~6
ZIF-8-derived ZnO ⁴⁰	300	1	6.7	1/28.5
FCN-MOSs (this work)	250	100	71.9	35/26

Nanoscale Paper

increases) based on the reaction of CH₃CH₂OH (gas) + 8O⁻ (ads) \rightarrow 3CO₂ + 3H₂O + 8e⁻. The ethanol molecules transfer electrons to the n-type (α-Fe₂O₃) or p-type material (such as CoFe₂O₄ and NiFe₂O₄ phases), leading to a decrease/increase in electrical resistance, respectively.

According to the literature, p-n sensing mode transition is mainly related to the work function variations caused by the targeted gases. 41 Kim et al. studied the p-n transition for CuO nanowires as a function of operating temperature for detecting the NO₂ gas. 42 In this study, the gas sensing transition from n-type to p-type is mainly due to the changes in the polarity of the sensing material, which means that the polarity of the sensing material can be changed from n-type to p-type when the phase composition of α-Fe₂O₃ (n-type) or CoFe₂O₄, and NiFe₂O₄ material (p-type) phases can be finely changed.

Conclusions

In summary, a series of Fe-MIL-88B-derived trimetallic FeCoNi oxides (FCN-MOS) were successfully synthesized using a onestep hydrothermal reaction with subsequent calcination treatment. The FCN-MOS system consists of α-Fe₂O₃, CoFe₂O₄, and NiFe₂O₄ and exhibits an elongated hexagonal rod-like structure with abundant mesopores. In addition, by altering the Fe, Co, and Ni ratio, the nanostructure and pore size of FCN-MOS can be effectively tuned, and a transition of gas-sensing behavior from n- to p-type can be achieved. The sensor based on FCN-MOS (Fe:Co:Ni = 7:1.5:1.5) exhibits excellent gassensing performance for ethanol, including high response (S =71.9), long-term stability (over 60 days), and good selectivity, as well as a low detection limit of 500 ppb. The unique mesoporous structure and synergic effects of the α-Fe₂O₃, CoFe₂O₄, and NiFe₂O₄ phases are primarily responsible for the enhanced sensing performance. Overall, this work provides a facile route for synthesizing MOF-derived metal oxide semiconductors and proposes a novel material design strategy.

Conflicts of interest

There are no conflicts to declare.

Acknowledgements

This work was supported by the National Natural Science Foundation of China (NSFC No. 41705098) and the International Exchange Grant (IEC/NSFC/201078) through the Royal Society and National Science Foundation of China (NSFC). This research was also supported by the Brain Pool program funded by the Ministry of Science and ICT through Research Foundation 2021H1D3A2A01100019). The authors would like to thank Kehui Han from Shiyanjia Lab (www.shiyanjia.com) for the xrd analysis.

References

- 1 D. P. Erdosy, M. B. Wenny, J. Cho, C. DelRe, M. V. Walter, F. Jiménez-Ángeles, B. Qiao, R. Sanchez, Y. Peng, B. D. Polizzotti, M. O. de la Cruz and J. A. Mason, Nature, 2022, 608, 712-718.
- 2 S. Zhou, O. Shekhah, A. Ramírez, P. Lyu, E. Abou-Hamad, J. Jia, J. Li, P. M. Bhatt, Z. Huang, H. Jiang, T. Jin, G. Maurin, J. Gascon and M. Eddaoudi, Nature, 2022, 606, 706-712.
- 3 S. Wang, W. Xie, P. Wu, G. Lin, Y. Cui, J. Tao, G. Zeng, Y. Deng and H. Qiu, Nat. Commun., 2022, 13, 6673.
- 4 H. K. Lee, C. S. Koh, W.-S. Lo, Y. Liu, I. Y. Phang, H. Y. Sim, Y. H. Lee, G. C. Phan-Quang, X. Han, C.-K. Tsung and X. Y. Ling, J. Am. Chem. Soc., 2020, 142, 11521-11527.
- 5 T. Devic and C. Serre, Chem. Soc. Rev., 2014, 43, 6097-6115.
- 6 C. Serre, C. Mellot-Draznieks, S. Surblé, N. Audebrand, Y. Filinchuk and G. Férey, Science, 2007, 315, 1828-1831.
- 7 P. Horcajada, F. Salles, S. Wuttke, T. Devic, D. Heurtaux, G. Maurin, A. Vimont, M. Daturi, O. David, E. Magnier, N. Stock, Y. Filinchuk, D. Popov, C. Riekel, G. Férey and C. Serre, J. Am. Chem. Soc., 2011, 133, 17839-17847.
- 8 W. Li, X. Guo, P. Geng, M. Du, Q. Jing, X. Chen, G. Zhang, H. Li, Q. Xu, P. Braunstein and H. Pang, Adv. Mater., 2021, 2105163.
- 9 M. Kim, R. Xin, J. Earnshaw, J. Tang, J. P. Hill, A. Ashok, A. K. Nanjundan, J. Kim, C. Young, Y. Sugahara, J. Na and Y. Yamauchi, Nat. Protoc., 2022, 17, 2990-3027.
- 10 V. Pascanu, G. González Miera, A. K. Inge and B. Martín-Matute, J. Am. Chem. Soc., 2019, 141, 7223-7234.
- 11 X. Wang, H. Xiao, A. Li, Z. Li, S. Liu, Q. Zhang, Y. Gong, L. Zheng, Y. Zhu, C. Chen, D. Wang, Q. Peng, L. Gu, X. Han, J. Li and Y. Li, J. Am. Chem. Soc., 2018, 140, 15336-
- 12 Q. Qian, Y. Li, Y. Liu, L. Yu and G. Zhang, Adv. Mater., 2019, 31, 1901139.
- 13 X. Xu, J. Liu, J. Liu, L. Ouyang, R. Hu, H. Wang, L. Yang and M. Zhu, Adv. Funct. Mater., 2018, 28, 1707573.
- 14 W. Xie, Y. Ren, B. Yu, X. Yang, M. Gao, J. Ma, Y. Zou, P. Xu, X. Li and Y. Deng, Small, 2021, 17, 2103176.
- 15 L. Lüder, A. Gubicza, M. Stiefel, J. Overbeck, D. Beretta, A. Sadeghpour, A. Neels, P. N. Nirmalraj, R. M. Rossi, C. Toncelli and M. Calame, Adv. Electron. Mater., 2022, 8, 2100871.
- 16 H. T. Jung, ACS Sens., 2022, 7, 912-913.
- 17 S. Y. Jeong, J. S. Kim and J. H. Lee, Adv. Mater., 2020, 32, e2002075.
- 18 A. Bag, M. Kumar, D.-B. Moon, A. Hanif, M. J. Sultan, D. H. Yoon and N.-E. Lee, Sens. Actuators, B, 2021, 346,
- 19 S. Cao, Y. Xu, Z. Yu, P. Zhang, X. Xu, N. Sui, T. Zhou and T. Zhang, Small, 2022, 2203715.
- 20 L. Wang, Y. Wang, H. Tian, L. Qiao and Y. Zeng, Sens. Actuators, B, 2020, 314, 128085.
- 21 W. Remlalfaka, C. Murugesan, P. N. Anantharamaiah and N. Manikanda Prabu, Ceram. Int., 2021, 47, 11526–11535.

Paper

22 N. Zhang, S. Ruan, F. Qu, Y. Yin, X. Li, S. Wen, S. Adimi and J. Yin, *Sens. Actuators, B*, 2019, **298**, 126887.

- 23 S. Zhang, W. Jiang, Y. Li, X. Yang, P. Sun, F. Liu, X. Yan, Y. Gao, X. Liang, J. Ma and G. Lu, *Sens. Actuators*, B, 2019, 291, 266–274.
- 24 T. Zhou, R. Zhang, Y. Wang and T. Zhang, *Sens. Actuators*, *B*, 2019, **281**, 885–892.
- 25 G. Lee, S. Lee, S. Oh, D. Kim and M. Oh, *J. Am. Chem. Soc.*, 2020, **142**, 3042–3049.
- 26 D. Bara, E. G. Meekel, I. Pakamore, C. Wilson, S. Ling and R. S. Forgan, *Mater. Horiz.*, 2021, 8, 3377–3386.
- 27 X. Zhang, G. Li, Y. Zhang, D. Luo, A. Yu, X. Wang and Z. Chen, *Nano Energy*, 2021, 86, 106094.
- 28 Z. Dai, C.-S. Lee, Y. Tian, I.-D. Kim and J.-H. Lee, *J. Mater. Chem. A*, 2015, 3, 3372–3381.
- 29 J. Chen, J. Zheng, Q. Huang, F. Wang and G. Ji, *ACS Appl. Mater. Interfaces*, 2021, **13**, 36182–36189.
- 30 H. B. Zheng, H. H. Chen, Y. L. Wang, P. Z. Gao, X. P. Liu and E. V. Rebrov, ACS Appl. Mater. Interfaces, 2020, 12, 45987–45996.
- 31 X.-Y. Huang, Z.-T. Chi, W. Yang, Y. Deng and W.-F. Xie, *Sens. Actuators, B*, 2022, **361**, 131715.
- 32 S. Sze and K. K. Ng, in *Physics of Semiconductor Devices*, 2006, pp. 5-75, DOI: 10.1002/9780470068328.ch1.

- 33 P. Wang, S. Z. Wang, Q. Han, D. Q. Zou, W. K. Zhao, X. D. Wang, C. Luo, X. Yang, X. Wu and W. F. Xie, Adv. Mater. Interfaces, 2020, 8, 2001831.
- 34 D. Xie, F. Zhang, G. Dai, Z. Mao, K. Yu and F. Qu, *New J. Chem.*, 2022, **46**, 11368–11376.
- 35 Y. Zhang, J. Zhang, G. Li, D. Leng, W. Wang, Y. Gao, J. Gao, Q. Liang, H. Lu and C. Wang, J. Mater. Sci.: Mater. Electron., 2019, 30, 17899–17906.
- 36 S. Wang, Z. Gao, G. Song, Y. Yu, W. He, L. Li, T. Wang, F. Fan, Y. Li, L. Zhang, X. Zhang, Y. Fu and W. Qi, *J. Mater. Chem. C*, 2020, 8, 9671–9677.
- 37 H. Sun, X. Tang, J. Zhang, S. Lia and L. Liu, *Sens. Actuators, B*, 2021, **346**, 130546.
- 38 J. H. Lee, T. T. T. Nguyen, L. H. T. Nguyen, T. B. Phan, S. S. Kim and T. L. H. Doan, *J. Hazard. Mater.*, 2021, 403, 124104.
- 39 Y. Tao and W. Zeng, Ceram. Int., 2021, 47, 8441-8446.
- 40 Y. Xia, A. Pan, D. W. Gardner, S. Zhao, A. K. Davey, Z. Li, L. Zhao, C. Carraro and R. Maboudian, *Sens. Actuators, B*, 2021, 344, 130180.
- 41 A. Gurlo, N. Bârsan, A. Oprea, M. Sahm, T. Sahm and U. Weimar, *Appl. Phys. Lett.*, 2004, **85**, 2280–2282.
- 42 Y.-S. Kim, I.-S. Hwang, S.-J. Kim, C.-Y. Lee and J.-H. Lee, *Sens. Actuators, B*, 2008, **135**, 298–303.